

**Dynamic pattern selection in polymorphic elastocapillarity**

Journal:	<i>Soft Matter</i>
Manuscript ID	SM-ART-09-2021-001376.R1
Article Type:	Paper
Date Submitted by the Author:	10-Nov-2021
Complete List of Authors:	Ha, Jonghyun; University of Illinois at Urbana-Champaign, Mechanical Science and Engineering Kim, Yun Seong; University of Illinois at Urbana-Champaign, Mechanical Science and Engineering Siu, Ryan; University of Illinois at Urbana-Champaign, Mechanical Science and Engineering Tawfick, Sameh ; University of Illinois at Urbana-Champaign, Mechanical Science and Engineering

Dynamic pattern selection in polymorphic elastocapillarity

Jonghyun Ha^a, Yun Seong Kim^a, Ryan Siu^a, and Sameh Tawfik^{*a,b}

^a Department of Mechanical Science and Engineering, University of Illinois at Urbana-Champaign, Urbana, Illinois 61801, USA. E-mail: tawfik@illinois.edu

^b The Beckman Institute for Advanced Science and Technology, University of Illinois at Urbana-Champaign, Urbana, Illinois 61801, USA.

Abstract

Drying of fine hair and fibers induces dramatic capillary-driven deformation, with important implications on natural phenomena and industrial processes. We recently observed peculiar self-assembly of hair bundles into various distinct patterns depending on the interplay between the bundle length and the liquid drain rate. Here, we propose a mechanism for this pattern selection, derive and validate theoretical scaling laws for the polymorphic self-assembly of polygonal hair bundles. Experiments are performed by submerging the bundles into a liquid bath, then draining down the liquid. Depending on the interplay between the drain rates and the length of the fibers, we observe the bundles morphing into star (having concave sides), polygons (having straight edges and rounded corners), or circles. The mechanism of self-assembly at the high drain regime is governed by two sequential stages. In the first stage of the high drain rate regime, the liquid covers the outside of the bundles, and drainage from inside the bundle does not play a role in the self-assembly due to the high viscous stress. The local pressure at the corners of the wet bundles compresses the fibers inward blunting the corners, and the internal lubrication facilitates fiber rearrangement. In the second stage, the liquid is slowly draining from within the fiber spacing, and the negative capillary pressure at the perimeter causes the fibers to tightly pack. In the slow drainage regime, the first stage is absent, and the fibers slowly aggregate without initial dynamic rearrangement. Understanding the mechanism of dynamic elastocapillarity offers insights for studying the complicated physics of wet granular drying.

1. Introduction

Drying of granular-like structures such as particles, hairs and fins plays a critical role in both natural phenomena, such as soil drying, and industrial processes, such as binder removal and capillary infiltration in material processing [1-4]. Hairs and long fibers have inherent flexibility due to their high aspect ratio, showing intriguing shape morphing and self-assembly. As an example of morphing hair in nature, otters, one of the semiaquatic mammals in the animal kingdom, utilize their hairs with cuticle patterns to trap air bubbles near their skin to regulate their body temperature during swimming [5]. Moreover, in nanomanufacturing, carbon nanotubes assemble and significantly deform, driven by capillarity, as they dry [6, 7]. This nanoscale self-assembly can be used to fabricate and tailor surface textures at high resolution and fast rates. In all of these processes, the kinetics play an important role on the final morphing shape of the hairs.

Capillary forces cause elastic deformation when a liquid meniscus forms between slender structures, a phenomenon known as elastocapillarity [8]. Here, balancing between bending and capillary energies gives the elastocapillary length, $l_{ec} \sim (B/\gamma)^{1/2}$, where B and γ are the bending stiffness per unit width and surface tension [9]. When the structure size is larger than l_{ec} , it gets deformed by capillarity. We

routinely observe elastocapillarity in our daily lives, such as painting, washing long hair, and drying of soils, wet grass or leaves [10]. Inspired by these intriguing phenomena, scientists have studied the deformation of flexible lamellae [11-14], and capillary rise in soft deformable solids [15-17].

Recently, our group and others observed that different self-assembly morphologies are observed as function of the rate of drainage. We have shown that hydrodynamic elastocapillary-driven assembly of hairy structures leads to bundle morphing into various patterns [18-22]. Currently, there are no theoretical scaling law models which can capture the drain rate dependence of the self-assembly patterns, also referred to as elastocapillary mode shapes. In particular, the mechanics of hairy bundles is extremely complex, exhibiting nonlinear packing leading to increase the resistance to compression [18]. This packing, in the case of hollow bundles, also controls the resistance to fluid flow through the bundles which sets the time scale of bundle morphing from an open bundle (having an internal hole) at low drain rate, to a closed bundle at high drain rate. However, for polygonal self-assembly, where there is no internal hole, it is not clear how the drain rate leads to dynamic pattern selection.

Here, we start with an experimental investigation of the multimodal self-assembly of prismatic bundles having triangular, square and pentagon cross sections. We then derive scaling laws to theoretically analyze the assembly modes driven by dynamic elastocapillarity. Considering the mechanics of packed hairs, we propose a nonlinear elastic force law and construct a theoretical model to predict the final shapes of the prismatic bundles emerging from the liquid with different drain rates. We finally compare the prediction model and the experimental measurements of elastocapillary deflections affected by drain dynamics.

2. Phenomenology of dynamic capillary morphing

A. Experimental observations

To investigate the polymorphic assembly of the polygonal hair bundles, we use a 3D printer (Micro Plus cDLM, Envisiontec) to fabricate various types of polygonal bases (triangle, square, and pentagon) having an array of holes forming a triangular, square or pentagon assembly, then insert individual carbon fiber tows with length l into the holes. The depth of the holes completely penetrates the base, and the fiber tows are fixed using an adhesive. A single carbon fiber tow has approximately 4600 fibers $2.5 \mu\text{m}$ in radius r . Since the bundles homogeneously swell when they are submerged in water, and the holes spacing is quite small, we can consider that they have uniform spacing d between the fibers. In the experiment, the radius of the polygons' circumcircle, distance from center to the polygon corners, is $R = 7 \text{ mm}$. The left side of Fig. 1 shows the schematics of the submerged prismatic hair bundles.

We submerge the bundles into a liquid bath, then pull them out from the liquid using a motorized linear stage (EAS series, Orientalmotor). Depending on the motor speed of the linear stage, we control the drain rates u ranging from 0.1 to 100 mm/s. We mount a DSLR camera on the top of the bundles to optically shoot the top view of the assembled bundles patterns. The top views of the initial and final shapes can be observed in the right to each schematic of Fig. 1. After drainage, the hairs of the bundles stick together by surface tension. For hair length $l > 10 \text{ mm}$, all hairs fully assemble, forming a star (concave polygon), polygon, and circle shapes as increasing u and l (see Fig. 1). We note that when l is very short ($l = 10 \text{ mm}$), the hairs cannot completely cluster together forming a hole in the center [23].

Short bundles (small l) or at slow drain rates (slow u), the bundles assemble into star shapes, with concave sides and relatively pointy corners. They form circle shapes when they are sufficiently long

(large l) and at fast drain rates (fast u). Between these two extremes, there is a transition regime where they form polygon shapes with straight sides and rounded corners. We plot the trend of assembly modes for various l and u on the right side of Fig. 1. As shown in Fig. 2(a), the final shapes transition from star to circle shapes as u increases even with the same bundle stiffness (same l). We observe that the bundles rearrange their configuration and become more circular at the early stage of the high drain rate regime (high u), as shown in Movie S1 and S2. In the following, we will discuss how the prismatic bundles assemble into various shapes due to both dynamical and geometrical effects.

First, to make the problem accessible by scaling laws, we propose a geometric parameter to describe the diversity of the self-assembly patterns. Taking symmetry into account, we consider a right-angle triangular unit cell in the polygons and quantitatively describe the geometry of the final shapes with this single numerical value, that we refer to as roundness s as shown in Fig. 2(b). The unit cell corresponds to the orange area in each polygon, as shown in the orange dashed lines of Fig. 2(b). As the number of sides of the polygons increases, the corner angle of the unit cell, θ , increases. Here, we geometrically simplify the final shapes of the unit cell, as shown in the black box of Fig. 2(b). Comparing two typical deflections: diagonal (hypotenuse of the unit cell) direction, δ , and the direction normal to the side of the polygon δ_n , we approximately describe the assembly mode shapes, where the roundness s can be written as

$$s = \frac{\delta \sin \theta}{\delta_n}. \quad (1)$$

The final shape is a star, polygon, or circle when $s < 1$, $s = 1$, and $s > 1$, respectively. We will theoretically derive scaling laws to calculate δ and δ_n of eqn (1) in detail in the next sections.

We experimentally measure δ and δ_n of the unit cell by averaging the values at every corner and side of the polygonal bundle. Using eqn (1), we plot s for various values of the drain rate u and bundle length l , as shown in Fig. 2(c). The plot uses darker shade of the markers' colors to visually show that s steadily increases when l or u increases. The assembled bundle tends to become more circular when $s > 1$, while it shows a star-like shape when $s < 1$. The bundles show a transition region of polygon shapes when $s \approx 1$. This simple but somewhat quantitative geometric analysis allows us to capture the self-assembly patterns. Final assembly patterns are spontaneously selected not only due to changes in u (dynamic effects) but also l (stiffness of bundles), as shown in the plots of Fig.1.

We note some characteristics of the s parameter and its sensitivity to the type of polygon. For triangles, as observed in Fig. 2(c), the s parameter is observed to (1) be numerically shifted to lower values, (2) show data spread over a wider range and (3) have a more "blurred" transition compared to more circular shapes like squares and pentagons. As shown in Fig. 2(c), the average value of the experimentally measured δ/δ_n is 0.9 when $l = 15$ mm and $u = 0.1$ mm/s (the smallest length and drain rate in the experiments). While having this same value of $\delta/\delta_n = 0.9$, we observe the difference in the calculated $s \approx 0.45, 0.63$, and 0.72 for the triangle, square, and pentagon, respectively. This can also be considered from the constant s perspective. For instance, $s = 1$ correspond to δ/δ_n of 2, 1.41 and 1.24 for triangle, square and pentagon respectively. Based on all these observations, a single numerical parameter, s , can typically capture the complex geometrical description of a wide variety of polygons and other shapes (stars and circles). We believe it greatly helps the mathematical modeling of the area of self-assembly of complex patterns.

Morphing mechanism

We find that the mechanism is best understood by considering the fast drain rate regime first. In the fast drainage regime, the assembly can be divided into two sequential processes: dynamic

rearrangement (stage 1), then slow capillary aggregation (stage 2), as shown in Fig. 2(a). Figure 3(a) provides schematic snapshots of the two morphing stages. As the bundles emerge from the bath, the hairs pierce the liquid interface without buckling and start to assemble. In stage 1, the liquid covers the outside of the bundles due to the high viscous stress between the small spacings of fibers while the horizontal liquid-air interface outside is freely descending at a velocity u . The sharp corners of polygonal bundles cannot maintain their small radius of curvature due to the local high Laplace pressure caused by the curvature. In this stage hence, the corners get blunted to release the corner's pressure, and compress the fibers inward. The liquid covering the bundle compresses the soft lubricated fibers by δ_d in the diagonal direction toward the centroid. This leads to dynamic rearrangement of the bundles where the initial spacing d_0 changes to d . The local pressure mostly acts on the corner, rather than the side, since the pressure difference can be negligible at the flat side of the bundle when it is covered with a thick liquid film (no menisci). Figure 2(a) shows that the lubricated bundles with the same l self-assemble into more circular configurations when the drain rate is fast. Because this initial rearrangement is the initial condition to the subsequent aggregation stage, stage 1 strongly influences the final shape observed after fast drainage even after the liquid is fully drained. Stage 2 takes a longer duration and starts after the initial dynamic rearrangement and the thick film covering the bundle drains. Capillary pressure in the menisci within the spacing between the fibers causes the bundles to shrink by δ_a at the corners, or δ_n on the flat sides to eventually form a star, polygon, or circle shape. Thus, the total deflection at the corner is $\delta = \delta_d + \delta_a$. Even in the fast drainage regime, stage 2 is slow, and it typically takes about 20 s for the liquid to drain and the final bundle geometry to form.

At slow drain rates, the liquid film around the bundles is constantly drained down under the force of gravity, unlike the fast drainage, and small menisci are left within the fiber spacings. From the in situ observations, we note that only stage 2, capillary aggregation, affects the assembly process, and stage 1 can be ignored. The negative pressure in the menisci between the fiber spacings along the perimeter of the bundle compresses the bundles inward from all directions. The rearrangement (stage 1) due to the dynamic effects does not affect the final pattern, and the assembly process directly starts from the aggregation step (stage 2). Thus, in the slow drainage regime, $\delta_d \approx 0$ and the total deflection can be written as $\delta \approx \delta_a$.

3. Scaling laws of hydrodynamic elastocapillary polymorphing

A. Capillarity forces exerted on the hair bundles

In stage 1, which only affects the fast drain rate experiments, a liquid film covers the perimeter of the polygonal bundles. At the corners, the local pressure tends to increase the radius of curvature and blunts the corners, as shown in Fig. 3(b). A dynamical capillary force, F_d , compresses the corners of the soft lubricated bundles. The local pressure difference driven by capillarity can be written as $p_1 - p_0 = \gamma/a$, where γ is surface tension and a is the radius of the curvature of the meniscus covering the corner. Here, we assume that the typical arc of the meniscus scales as a . Then, we can typically set the surface area as ah , where h is an external rise height raised by the drain dynamics. Multiplying the surface area and the local pressure, we obtain

$$F_d \sim \gamma h, \quad (2)$$

as shown in the black box of Fig 3(a). The external rise height, h , arises at the outermost fibers when the bundles emerge from the water bath. According to the classical model for h (Landau-Levich film problem), we can express the characteristic length $h \sim l_c \text{Ca}^{1/3}$ [24]. l_c is the capillary length of the liquid used, $l_c = (\gamma/\rho g)^{1/2}$, where ρ and g are the density of the liquid and gravitational acceleration, respectively. Ca is the capillary number, $\text{Ca} = \mu u/\gamma$, where μ is liquid viscosity. Using $h \sim l_c \text{Ca}^{1/3}$, eqn (2) yields $F_d \sim$

$\gamma^{7/6}(\rho g)^{-1/2}(\mu u)^{1/3}$. This force leads to a deformation δ_d at the corners. The stiffness relating the force to the deformation is described in the next section. At fast u , the soft lubricated bundles become circular due to the large magnitude of F_d , as shown in the bottom images of Fig. 3(b). This is associated with fiber rearrangement leading to changing the shape of the unit cell. We approximate this shape change as shown in Fig. 3(c), by deriving the relation of the new corner angle, θ_d . Using the sine rule, we mathematically write

$$\theta_d = \tan^{-1} \left[\frac{R \sin \theta \cos \theta}{R(\cos \theta)^2 - \delta_d} \right]. \quad (3)$$

According to eqn (3), $\theta_d \approx \theta$ when δ_d is very small (slow u). We note that h , the external film height, is valid only within stage 1. At the end of this stage, the liquid film surrounding the bundle is completely drained. Once the liquid starts to drain through the fiber spacing (stage 2), h is not valid. We indeed rationalize a characteristic time scale relevant only for the early stages of the rearrangement governed by $h \sim l_c Ca^{1/3}$, at the fast drainage regime. Using this h scaling, the characteristic growth time scale of the external rise height is expressed as $\tau \sim h/u$, so $\tau \sim \gamma^{1/6}(\rho g)^{-1/2} \mu^{1/3} u^{-2/3}$. We compare the theoretically predicted τ with the experimentally measured rearrangement time, as shown in Fig. 4(a). The plot of Fig. 4(b) shows that the rearrangement time scale obeys the relation $u^{-2/3}$. Based on this result, one can accept that the Landau-Levich problem governs the characteristic time scale of the external dynamic rise and the dynamic rearrangement, which is relevant in the early stage of the fast drainage regime.

Next, the assembly proceeds to stage 2: capillary aggregation of the hairs. While the liquid continues to slowly drain from within the bundles, the meniscus between the fibers leads to the capillary pressure acting perpendicular to the polygon sides. Thus, the capillary pressure can be expressed as γ/b , where b is the radius of the curvature of the meniscus between the fibers, as shown in Fig. 3(c). This compression pressure is applied to total fiber length l so that the surface area can be scaled as bl . Multiplying the pressure and the surface area, we obtain the side compression force, $F_c \sim \gamma l$. At the corner, especially, the compression in a diagonal direction is scaled as $\gamma l \sin \theta_d$ by considering the bundle geometry after fiber rearrangement, as shown in the black box of Fig. 3(c). We note that the resulting deformation due to aggregation has different values in the corners δ_a than the side δ_n not only due to the different force, but also due to different stiffness as described in the next section.

B. Nonlinear restoring stiffness of the bundles in the aggregation stage

First, we consider the nonlinear stiffness of a fiber array where each fiber is treated as a cantilever, and the stiffness of the array is governed by the fibers progressively making contact as the deformation is increased. The fibers are wet; so this case is relevant for the hydrodynamically lubricated fibers. The elastic deflection of a single soft rod obeys the classical Hooke's law, where the deflection is linearly proportional to the elastic force. However, the situation will be qualitatively different when the row of hairs, having initial spacing d , sequentially come into contact, as shown in Fig. 5(a). When the deformation is larger than d , the total deflection can be expressed as $\delta_a \sim nd$, where n is the number of fibers coming into contact. When all hairs in a row are in contact but still lubricated, we sum all individual fiber deflection to express the elastic resistance force:

$$F = \frac{EI}{l^3} \left[\delta_a + \sum_{i=1}^{n-1} (\delta_a - id) \right], \quad (4)$$

where i is integer numbers ranging from 1 to $n - 1$. E and I are Young's modulus and second moment of area of a single rod, respectively. The summation equation of eqn (4) yields

$$F = \frac{EI}{l^3} \left[\delta_a n - \frac{dn(n-1)}{2} \right]. \quad (5)$$

Using the relation $\delta_a \sim nd$, eqn (5) becomes

$$F \sim \frac{EI}{dl^3} \delta_a^2, \quad (6)$$

when $n \gg 1$ [18,19]. Since the deformation is typically larger than the spacing d , as shown in Fig. 5(b), we use this quadratic force law ($F \propto \delta_a^2$), instead of the linear force law.

Due to the inward nature of the capillary forces, the bundle stiffness is also governed by packing effects. This especially affects the diagonal direction where fibers from the side tend to deposit in the diagonal direction due to the large deformation of the bundle's cross section. The packing effects lead to a nonlinear stiffness law due to elimination of internal voids. Specifically, in both the initial and final packing configurations of the unit cell, the bundle has internal voids. However, the decrease in these voids due to aggregation causes significant stiffening effect due to packing. It is important to model the packing-induced stiffening by considering the fiber rearrangement. The rearrangement is driven by the capillary forces between individual fibers which pulls the fibers closer together as the bundle deforms (see Fig. 5(b)). Hence, the direction of the capillary forces changes with the bundle deformation, a phenomenon known in solid mechanics as “follower forces”, defined here as forces which change their absolute direction due to large deformation [25]. Under the effect of follower forces, the fibers in the “diagonal” direction provide larger resistance to deformations due to rearrangement. The black box of Fig. 5(c) schematically shows the expected packing configuration of the assembled bundles, where rows of fibers, acting like parallel springs, resist the deformation in the diagonal direction. We mathematically derive a force law for the packed bundle due to aggregation at the corners (see Appendix A for details). The restoring force of the bundle in the diagonal direction is:

$$F_a \sim \left(\frac{\rho_0 R}{\rho_f r R - \delta} \sin \theta \cos \theta \right) \frac{EI}{dl^3} \delta_a^2. \quad (7)$$

The predictive expression of eqn (7) resembles eqn (6) but has the effect of large changes in packing in the pre-factor of the right hand side. In this pre-factor, ρ_0 and ρ_f are the dimensionless initial and final area fraction of fibers (as observed from the top), which have values of 0.089 ± 0.006 and 0.37 ± 0.11 , respectively as measured experimentally. Figure 4(d) shows the difference between quadratic force law with and without packing effects, by theoretically comparing eqn (6) and (7). As expect, the significant stiffening is due to the terms $R/r \sim 10^3$ and the packing causes increased stiffening as governed by the term $R - \delta$ in the denominator. We find that the packing force law is critical to capture the pattern selection in elastocapillarity of prismatic hair bundles.

4. Nonlinear capillary force-deflection relations

We derive the dynamic deflection δ_d , relevant for the fast drainage regime (high u). In this stage, we treat the bundles as soft noninteracting beams with lubricated interfaces. The elastic resistance of the soft floppy bundles having N fibers can be simply expressed as $F_s = NEI/l^3 \delta_d$. The details of the expression of N are in Appendix A. Using the dynamic capillary force F_d of eqn (2), the force balance ($F_s \sim F_d$) leads to $\gamma h = NEI/l^3 \delta_d$. Please note that the external rise height can be written as $h \sim l_c(\mu u/\gamma)^{1/3}$ being a function of u , so δ_d can be neglected when u is very small. Based on this force balance, the normalized deflection due to dynamic effects $\bar{\delta}_d = \delta_d/R$ can be theoretically written as

$$\bar{\delta}_d = \alpha_d (\lambda \eta \phi)^2 \zeta, \quad (8)$$

where $\alpha_d = r/(k\rho_0 R)$, $\lambda = l/R$ is the aspect ratio, $\eta = l/l_{ec}$ is the elastocapillary number, and $\phi = (\cos \theta)^{-1/2}$

is the roundness factor of the polygon, where the polygonal shapes become close to a rounded shape as θ increases. k is a prefactor for the scaling law. The dimensionless external rise height, $\zeta = h/l(\sin\theta)^{-1}$ being a function of u , indicates the magnitude of the dynamic effects.

In stage 2, the rearranged bundles undergo further deformation due to fiber aggregation. In this stage, the capillary compression in the diagonal direction ($F_c \sin\theta_d$) is balanced by F_a of eqn (7), such that we can write $\gamma/\sin\theta_d = [(\rho_0/\rho_f)(R/r)R/(R-\delta)\sin\theta\cos\theta]EI/(d^3)\delta_a^2$, where $\delta = \delta_d + \delta_a$. We rearrange the preceding relation in terms of δ_a , make some simplifications (see Appendix B for details), then normalize such that $\bar{\delta}_a = \delta_a/R$, and finally obtain

$$\bar{\delta}_a = \frac{[\{\alpha_a(\lambda\eta\phi)^2\}^2 + 4\alpha_a(\lambda\eta\phi)^2(1 - \bar{\delta}_d)]^{1/2} - \alpha_a(\lambda\eta\phi)^2}{2}, \quad (9)$$

where $\alpha_a = \rho_d d_0/(\rho_0 R)$. The quadratic solution of eqn (9) is nonlinear function of the term $\lambda\eta\phi$ due to packing effects. We note that the aggregation model of eqn (9) includes $\bar{\delta}_d$ of eqn (8) since stage 2 starts from the dynamically rearranged bundles resulting from stage 1. If the dynamic effects are absent ($\bar{\delta}_d = 0$), the assembly is mainly governed by static capillarity.

In stage 2, the deflection in the normal direction is determined solely by the geometry, where the capillary force simply pull the fibers inward until they fully densify with no void between them. Here, we do not consider rearrangement-induced packing because of the flat nature of the side, in contrast with the corner, as shown in the green box of Fig. 5(b). Back of the envelope calculation support this treatment as mentioned in the Appendix C. The value of δ_n can be estimated by a geometric argument by considering the elimination of spacing between the fibers in the densified state, leading to $\delta_n \approx R d_0/(r + d_0)\sin\theta$. Normalizing δ_n by R gives

$$\bar{\delta}_n = \frac{d_0}{r + d_0} \sin\theta. \quad (10)$$

We note that eqn (10) does not depend on capillary forces, since it is derived based on the geometric arguments of full densification (see Appendix C for detail). Based on eqn (8), (9) and (10), the final deformed shape of the polygon can be estimated as described in the next section.

5. Scaling prediction of the dynamic pattern selection

We have theoretically investigated the deflections in the diagonal and normal directions so far. For the diagonal direction, we express $\bar{\delta} = \bar{\delta}_d + \bar{\delta}_a$ by combining eqn (8) and (9). The normal direction can be expressed in eqn (10). Based on eqn (1), theoretically predicted s can be written as

$$s = \frac{2\alpha_a(\lambda\eta\phi)^2\zeta + [\{\alpha_a(\lambda\eta\phi)^2\}^2 + 4\alpha_a(\lambda\eta\phi)^2\{1 - \alpha_a(\lambda\eta\phi)^2\zeta\}]^{1/2} - \alpha_a(\lambda\eta\phi)^2}{2^{d_0}/(r + d_0)}. \quad (11)$$

The theoretical model of eqn (11) involves the polygon shape roundness (ϕ), bundle aspect ratio (λ), elastocapillarity effect (η), and fluid dynamic effects (ζ). Using these dimensionless parameters, we transform the regime map in the plots of Fig. 1 into a universal regime map (ζ versus $\lambda\eta\phi$) in Fig. 6. According to Fig. 2(c), the range below $s = 1$ indicates that the final shapes of bundles are star. When $s \approx 1$ (transition regime), the bundles assemble to polygonal shapes. Finally, they select circular patterns when s exceeds 1. In Appendix D, we mathematically describe an exact value of s corresponding to transforming each bundle type (triangle, square, pentagon) to a corresponding regular bundle that is more rounded. As shown in Fig. 6, one observes theoretical curves for various s ranging from 0.9 to 1.1, corresponding to three dynamic assembly modes. We note that the theoretical curves asymptotically

converge to the dashed line in Fig. 6, where $\zeta \sim 1/[\alpha_d(\lambda\eta\phi)^2]$ when $s \geq 1.2$. It shows the star shapes at small $\lambda\eta\phi$ and ζ , which corresponds to high stiffness and negligible dynamic effects. The middle range of $\lambda\eta\phi$ and ζ is the transition region, where the bundles morph to the polygons. Finally, the bundles become circular in the range of high $\lambda\eta\phi$ and ζ , which corresponds to large flexibility and dominant dynamic effects.

When $\lambda\eta\phi$ is very small ($\lambda\eta\phi < 4$), an internal void forms in the bundle due to the strong stiffness even in high ζ (see Fig. 6). Using the preceding model [11], we can roughly estimate the typical threshold of maximum bundle size following the fiber length: $N_t = \beta[l^2/(l_{ec}d)]^{2/3}$, where β is a prefactor for the scaling law. The total number of fibers of the polygon bundle can be written as $N_t = cN$, where $c = 2\pi/(\pi/2 - \theta)$ is the number of the unit cell in polygons. When the polygon is a triangle, for example, $c = 6$. Based on the relation N_t , we can express the minimum $\lambda\eta\phi$ to completely assemble whole fibers,

$$(\lambda\eta\phi)_m = \frac{1}{\beta^3} \left[\frac{c^3 R^2 \sin^3 \theta \cos \theta}{d_0^2} \right]^{1/4}. \quad (12)$$

The typical $(\lambda\eta\phi)_m$ of eqn (12) by averaging the three polygons (triangle, square, and polygon) is approximately 4, when $\beta = 2.6$ (see the vertical dashed line of Fig. 5(b)). Only when $\lambda\eta\phi > (\lambda\eta\phi)_m$, the bundles show complete fiber assembly into a single solid bundle, which is our main interest.

6. Conclusions

We have theoretically and experimentally investigated the polymorphic assembly of hairy bundles by dynamic elastocapillarity. We experimentally show that prismatic hair bundles exhibit various shapes after assembly due to the interplay between their stiffness (fiber length) and dynamic capillary aggregation. By combining in situ experiments and theoretical scaling laws, we explain the mechanism of pattern selection as follows. At fast drainage, the liquid initially covers the bundles due to the high viscous stress in the spacing between the fibers. The fibers are rearranged by the local pressure at the corners of soft lubricated bundles due to the presence of thick liquid films on the perimeter. After this fast rearrangement, the liquid starts to drain down slowly from the inner parts of the fibers and menisci appear around the perimeter, then capillary pressure between the fibers compresses the bundles and cause them to aggregate and pack. On the other hand, in the slow drainage regime, the dynamic effects can be ignored, and the fibers directly aggregate without rearrangement. To construct a scaling law to describe this mechanism, we modeled the packing effects at the corner of the polygonal bundles during the assembly, which lead to a nonlinear elastic force law. We propose a simple geometric descriptor, referred to as the roundness s , to describe the bundles' final shapes, namely stars, polygons, and circles. We non-dimensionalize the various factors affect the self-assembly, namely the polygon shapes (ϕ), bundle lengths (λ), elastocapillary effects (η), and fluid dynamic effects (ζ). Using these dimensionless parameters, we theoretically expressed the deflections in both diagonal and normal directions of the unit cell, then provide a universal regime map of morphing polygonal bundles, as shown in Fig. 6. Our theoretical model captures three distinct assembly modes for various $\lambda\eta\phi$ and ζ well. We expect that the present work will be useful for soft matter fields concerned with predicting complex morphing geometries such as flexible membranes [26,27], nano/microfabrication [28,29], programmable origami [30,31], and even some applications of soft robotics and actuators [32,33].

Appendix A: Nonlinear stiffness due to packing effects

Fiber aggregation leads to packing-induced nonlinear and non-isotropic stiffening. Due to the geometry of the polygonal bundles, and the nature of the capillary forces acting inward in a direction perpendicular to the sides, packing is non-uniform within the bundle area. Consider for instance a single isolated row of fibers oriented in the diagonal direction before shrinkage. After shrinkage, the row can not be considered as a single row because fibers come into contact forming multiple rows, n_a , acting like springs in parallel, in the diagonal direction (see the bottom black box of Fig 4(c)). Then, the total elastic force can be simply expressed, $F_a = n_a F$, to consider n_a parallel rows acting like springs in parallel to resist deformation in the diagonal direction. Figure 4(c) shows the packing morphology of the assembled bundles. In an initial configuration of the unit cell, the area occupied by fibers can be written as $\rho_0 R^2 \sin \theta \cos \theta / 2$, where the dimensionless number ρ_0 is the initial top area fraction of fibers. Using the top area of the bundle ($Nr^2\pi$), the total number of fibers of the unit cell can be written as

$$N \sim \frac{\rho_0 R^2 \sin \theta \cos \theta}{r^2}. \quad (\text{A1})$$

Here, we use the scaling law $\text{sign} \sim$ and ignore the constant numbers such as integer and π . After assembly, we can typically write the assembled area occupied by fibers, $\rho_f(R - \delta)rn_a$. Fiber area conservation, $Nr^2\pi = \rho_f(R - \delta)rn_a$, allows us to express $n_a \sim Nr/[\rho_f(R - \delta)]$. Replacing N with eqn (A1) yields

$$n_a \sim \frac{\rho_0 R^2}{\rho_f r (R - \delta)} \sin \theta \cos \theta. \quad (\text{A2})$$

Using eqn (A2) and (6), we can express the total elastic resistance, $F_a = n_a F$, as eqn (7). This packing-induced stiffening in the diagonal direction is critical to form the star shapes with pointy corners.

Appendix B: Deflection due to capillary aggregation, δ_a

Balance between capillary compression ($F_c \sin \theta_d$) and elastic resistance (F_a) leads to $\gamma l \sin \theta_d = [(\rho_0/\rho_f)(R/r)R/(R-\delta)\sin \theta \cos \theta]EI/(dl^3)\delta_a^2$. We rearrange the preceding relation in terms of δ_a , then the equation becomes

$$\delta_a^2 = \frac{\rho_f d l^4}{\rho_0 R EI / (r\gamma) \cos \theta} \frac{1}{R} \frac{R - \delta \sin \theta_d}{d_0 \sin \theta}. \quad (\text{A3})$$

The last fraction of eqn (A3), $d \sin \theta_d / (d_0 \sin \theta)$, depends on dynamic effects, but its variance is negligible in the current experimental range. Therefore, we can simplify eqn (A3) to the normalized expression:

$$\bar{\delta}_a^2 = \alpha_a \left(\frac{l}{l_{ec}}\right)^2 \left(\frac{l}{R}\right)^2 \left(\frac{1}{\cos \theta}\right) (1 - \bar{\delta}), \quad (\text{A4})$$

where $\alpha_a = \rho_f d_0 / (\rho_0 R)$ and $l_{ec} = [EI/(r\gamma)]^{1/2}$. We note that $\bar{\delta} = \bar{\delta}_a + \bar{\delta}_d$. By solving a quadratic equation of eqn (A4), then normalizing $\bar{\delta}_a = \delta_a/R$, we obtain eqn (9).

Appendix C: Approximate solution of deflection in normal direction, δ_n

In the normal direction, the fibers can easily contact without significant jamming effects the compression force and the fiber displacement are aligned, as shown in the green box of Fig. 5(b). We consider δ_n being solely a function of geometry. According to the elimination of the spacing d within the fibrous array, we get $\delta_n = n_n d$, where n_n is the number of the fibers at the single row in the normal direction. Dividing the side length of the unit cell by the spacings and fiber radius, $n_n = R \sin \theta / (r + d)$.

Normalized δ_n by R can be written as

$$\bar{\delta}_n = \frac{d}{r+d} \sin \theta. \quad (\text{A5})$$

We can estimate the decrease in d by the conservation of N between the initial and rearranged configuration (stage 1 as illustrated in Fig 3(a)):

$$d = d_0(1 - \bar{\delta}_d)^{1/2}. \quad (\text{A6})$$

One can geometrically accept that d of eqn (A6) will decrease as the bundle shrinks and rearrange by δ_d . The magnitude of change of $\bar{\delta}_n$ in eqn (A5) is very small, so we approximately use $\bar{\delta}_n$ of eqn (10) being a function of geometrical parameters. As a final note, the deflection balancing between F_c and F of eqn (6) can be written as $\delta_a \sim [\gamma^4 d / (EI)]^{1/2}$. Thus, $\delta_a \approx 166$ mm when $l = 20$ mm. A typical $\delta_n \approx 3$ mm in a triangle configuration, so $\delta_n \ll \delta_a$, allows us to assume that the fibers will stop deforming once they are all in contact. Due to the symmetry between the different unit cells, they all then balance each other, and the bundle remains straight without much more densification.

Appendix D: Mathematical description of circular patterns

We geometrically express circular shapes using the s parameter by considering the transformation of each unit cell to a regular unit cell, and hence the same number of unit cells forming a regular polygon, as shown in Fig. 7. Considering a triangular bundle for instance which had six right-angled unit cells before self-assembly, the final shape after self-assembly becomes a regular hexagon since each of the triangular unit cell becomes isosceles. The initial bundles having triangle, square, and pentagon cross sections transform their cross section to a circle, which we approximate mathematically as hexagon, octagon, and decagon, respectively. We write the area of the gray isosceles triangle in the inset of Fig. 7: $w^2 \cos \theta / 2$, where w is the radius of the circumcircle of the regular polygon. By using N of eqn (A1), the fiber area conservation, $Nr^2 \pi = \rho w^2 \cos \theta / 2$, yields

$$w \sim \left(\frac{\rho_0}{\rho_f} \sin \theta \right)^{1/2} R. \quad (\text{A7})$$

Considering the ratio of deflections in the diagonal and normal directions, we can mathematically express the roundness for the circular shapes:

$$s_w = \frac{(R-w) \sin \theta}{R \sin \theta - w}. \quad (\text{A8})$$

The values s_w of eqn (A8) are 2.1, 1.4, and 1.2 for triangle, square, and pentagon, respectively. This geometrical argument is mathematical more rigorous than simply considering the onset of circularity to be $s > 1$. Interestingly, we find that when $s > 1.2$, ζ reaches an asymptotic scaling of $\zeta \sim 1 / [\alpha_d (\lambda \eta \phi)^2]$.

Acknowledgement

This work was supported by AFOSR Young Investigator Program (Grant No. FA9550-19-1-0010), NSF CMMI (Grant No. 1825758).

Figures

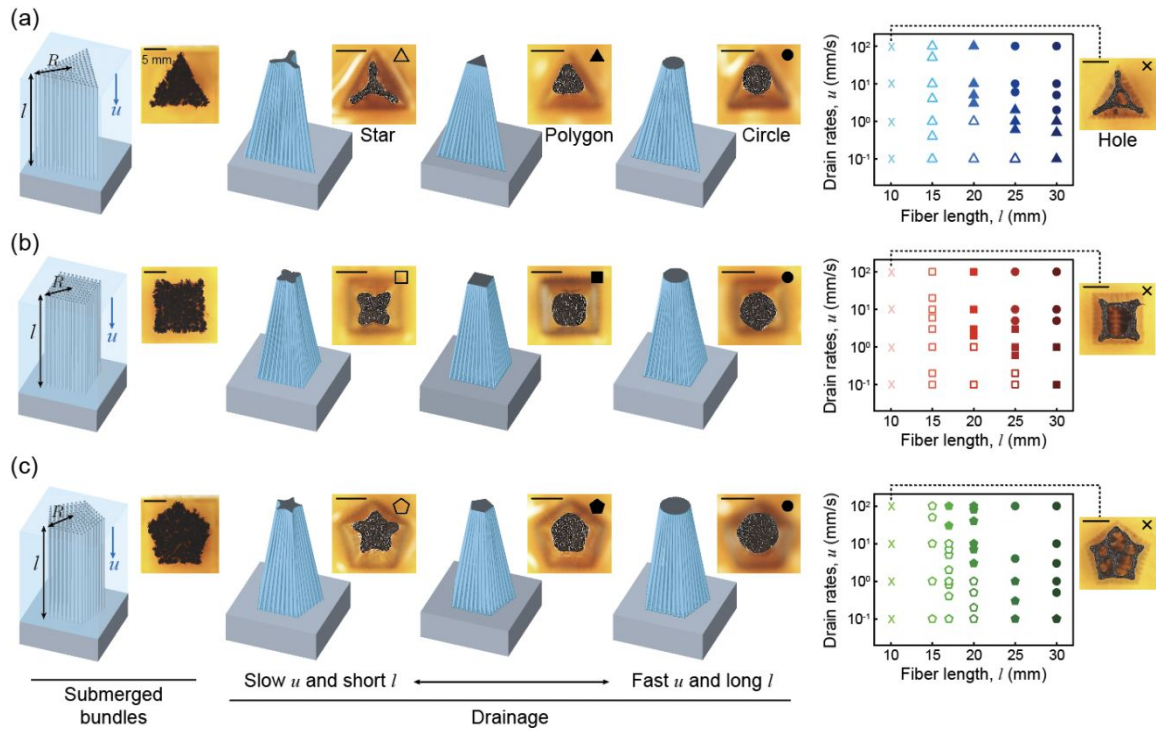


Fig. 1. Dynamic pattern selection in polymorphic elastocapillary of prismatic hair bundles having (a) triangular, (b) square, and (c) pentagon cross section. The schematics on the left side of (a,b, and c) show the submerged bundles, and the rest show the bundles having different final patterns after complete drainage. The experimental top view photographs of the bundles are located at the right side of each 3D schematics. In the plots, empty polygons, filled polygons, and circles correspond to star, polygon, and circle shapes, respectively. The symbol \times corresponds to bundle self-assembly with a hole forming at the center. The darkness of the symbols indicates the increase in the original bundle length l , for the same bundle size $R = 7$ mm. Movie S1 shows the assembly videos of three modes (star, polygon, and circle) in three polygons (triangle, square, and pentagon). All scale bars are 5 mm.

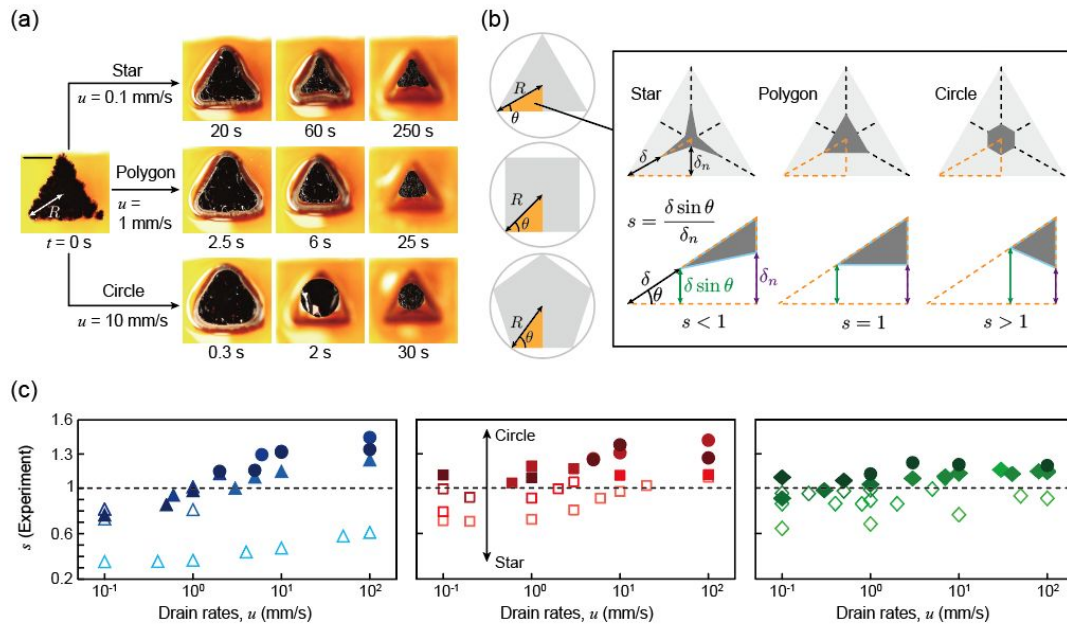


Fig. 2. Geometric parametrization of polymorphic assembly of polygonal bundles. (a) The morphology of the assembled bundles in various drain rates when $l = 25$ mm and $R = 7$ mm (see Movie S2). scale bar is 5 mm (b) Description of the final shapes of the triangular bundles. The angle θ of the orange region is different for each type of polygon, but the bundles are design to have the same R . The black frame shows the geometric parametrization of the assembly modes by the roundness, s . Orange dashed lines correspond to the unit cell of polygons. (c) Experimentally measured s versus u for various geometries. All symbols are listed in the plots of Fig. 1.

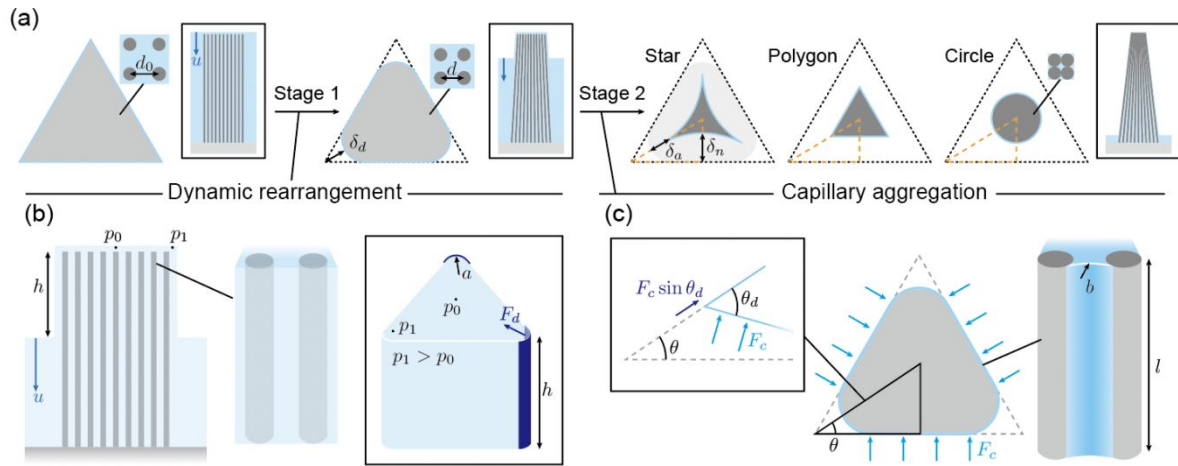


Fig. 3. Mechanism of capillary compression of polygonal bundles. (a) General mechanism of bundle morphing during the drainage showing the two stages of the fast drainage; whereas only stage 2 plays a role in the slow drainage. The bundles are rearranged by δ_d due to the dynamic effects and then further shrink by δ_d in a diagonal and δ_n in a normal direction. The black boxes indicate the side view of the bundles in the assembly process. The dashed orange lines correspond to the unit cell of the triangles. (b) Forces during the dynamic rearrangement of stage 1. Schematics of the external dynamic rise height induced by u . The black box shows the force blunting the corners F_d operating along height h . (c) Fiber aggregation during stage 2 is governed by capillary pressure, γ/b , between the fibers. The black box shows the close-up view of the compression direction at the corner, considering the evolution of the morphology after stage 1.

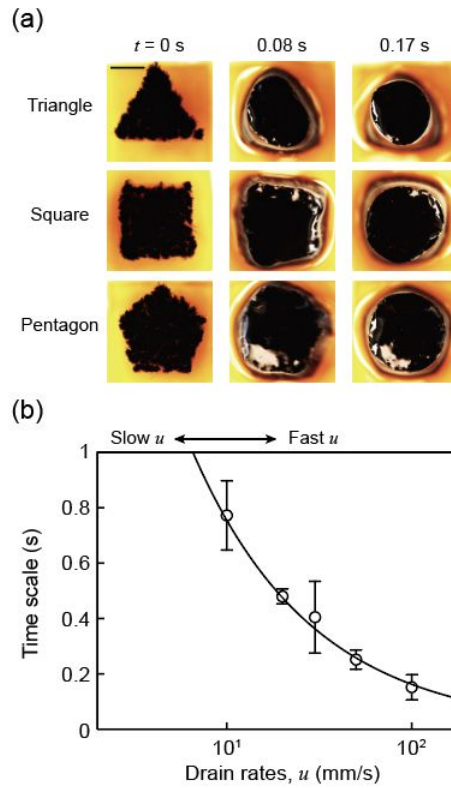


Fig. 4. The characteristic timescale of the rearrangement. (a) Optical images showing the top view of the polygons at the onset, middle and end of the rearrangement stage in the fast drainage regime. All three bundles have $l = 25$ mm and drain rate $u = 100$ mm/s. (b) Comparison between experimentally measured rearrangement time (open symbols) and theoretically predicted growth time (black line). The black theoretical line is $\tau = ch/u$, where $c = 5.5$ is a prefactor of the scaling law to precisely fit the experiments. The error bars of the data correspond to the standard deviation of all experimental measurements at each drain rate.

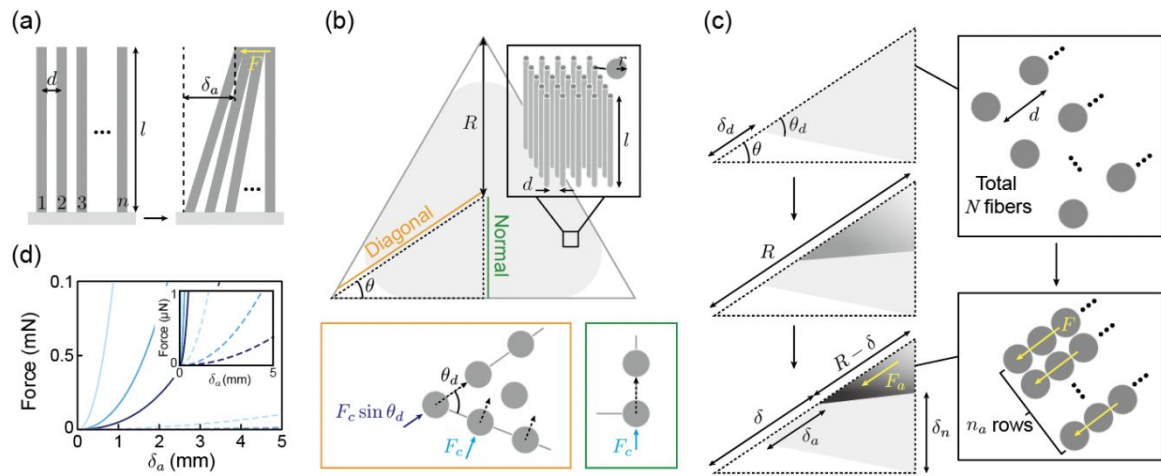


Fig. 5. Nonlinear elasticity of the hair bundles. (a) Description of F , the restoring force of a single array having n fibers. (b) The geometry of the various directions of forces and fiber deformations. The black box shows a close-up view of triangular bundles after rearrangement. The orange and green boxes correspond to the fiber aggregation in the diagonal and normal directions, respectively. The black dashed arrows correspond to the movement direction of fibers. (c) Capillary aggregation with packing effects in the diagonal direction. The darkness of the gray tones indicates increased packing and stiffness. The black boxes on the right illustrate the fibers in the diagonal direction before (top) and after (bottom) packing. n_a is an effective row size perpendicular to the diagonal direction. (d) Comparison between quadratic force laws with packing effects (solid lines) and without them (dashed lines). The line colors in order from light to dark correspond to $l = 10, 20,$ and 30 mm. In the computation, we exclude the dynamic effects ($\delta_d = 0$) and use $\theta = 30^\circ$ (triangle).

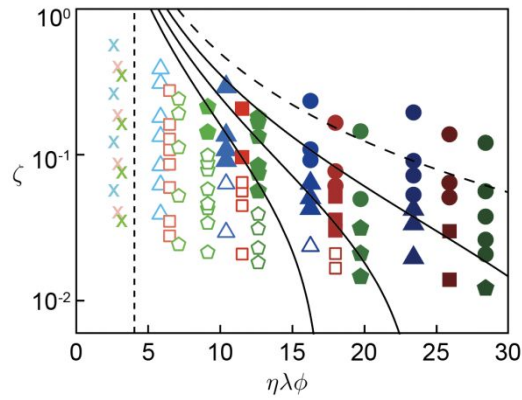


Fig. 6. Regime map of the assembly patterns selection. The theoretical lines of eqn (10) in order from left to right are $s = 0.9$, 1 , and 1.1 . The vertical dashed line corresponds to the minimum $\lambda\eta\phi$ for complete assembly, expressed by eqn (11). All symbols are listed in the plots of Fig. 1. In the computation, $k = 0.2$. Most of the bundles that self-assemble into starts (open markers) fall to the left of the $s = 0.9$ curve, while most of the bundles that form circular shapes are to the right of the $s = 1.1$ curve. The dashed line corresponds to the asymptotic solution reached when $s \geq 1.2$, and corresponds to the asymptotic solution, $\zeta \sim 1/[\alpha_d(\lambda\eta\phi)^2]$.

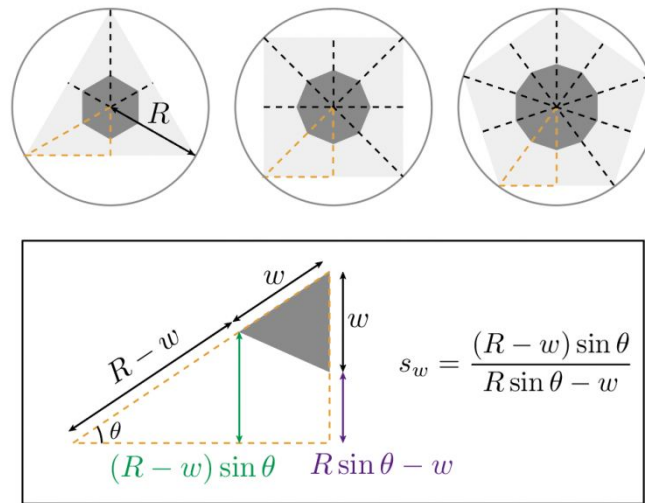


Fig. 7. Mathematical description of the circular patterns in each polygon. The regular polygons of hexagon, octagon, and decagon correspond to the circular patterns in triangle, square, and pentagon, respectively. Orange dashed lines corresponds to the unit cell. The inset indicates s of the circular patterns can be expressed by w , R and θ .

References

1. D. Or, P. Lehmann, E. Shakraeni, N. Shokri, *Vadose Zone J*, 2013, **12**, vzj2012-0163.
2. N. H. Ceaglske and O. A. Hougen, *Ind. Eng. Chem.*, 1937, **29**, 805-813.
3. J. A. Lewis, *Annu. Rev. Mater. Sci.*, 1997, **27**, 147-173.
4. A. Mostafaei, A. M. Elliott, J. E. Barnes, F. Li, W. Tan, C. L. Cramer, P. Nandwana, and M. Chmielus, *Prog. Mater. Sci.*, 2021, **119**, 100707.
5. J. W. Weisel, C. Nagaswami, and R. O. Peterson, *Can. J. Zool.*, 2005, **83**, 649.
6. S. Tawfick, J. Bico, and S. Barcelo, *MRS Bull.*, 2016, **41**, 108-114.
7. M. Volder, S. Tawfick, S. J. Park, D. Copic, Z. Zhao, W. Lu, and A. Hart, *Adv. Mater.*, 2010, **22**, 4384.
8. J. Bico, É. Reyssat, and B. Roman, *Annu. Rev. Fluid Mech.*, 2018, **50**, 629.
9. A. Cohen and L. Mahadevan, *Proc. Natl. Acad. Sci. USA*, 2003 **100**, 12141.
10. C. Duprat, S. Protière, A. Beebe, H. A. Stone, *Nature*, 2012, **482**, 510.
11. J. Bico, B. Roman, L. Moulin, A. Boudaoud, *Nature*, 2004, **432**, 690.
12. H.-Y. Kim and L. Mahadevan, *J. Fluid Mech.*, 2006, **548**, 141.
13. J. M. Aristoff, C. Duprat, H. A. Stone, *Int. J. Nonlin. Mech.*, 2011, **46**, 648.
14. C. Duprat, J. Aristoff, H. A. Stone, *J. Fluid Mech.*, 2011, **679**, 641.
15. J. Ha, J. Kim, Y. Jung, G. Yun, D.-Y. Kim, and H.-Y. Kim, *Sci. Adv.*, 2018, **4**, eaao7051.
16. D. P. Holmes, P. T. Brun, A. Pandey, S. Protière. *Soft Matter*, 2016, **12**, 4886.
17. B. Nasouri, B. Thorne, and G. J. Elfring, *J. Fluid Struct.*, 2019, **85**, 220-228.
18. J. Ha, Y. S. Kim, K. Jiang, R. Siu, and Tawfick, *Phys. Rev. Lett.*, 2020, **125**, 254503.
19. D. Shin and S. Tawfick, *Langmuir*, 2018, **34**, 6231.
20. L. Kovanko and S. Tawfick, *Langmuir*, 2019, **35**, 13421.
21. A. Hadjittofis, J. R. Lister, K. Singh, and D. Vella, *J. Fluid Mech.*, 2016, **792**, 168-185.
22. N. Chakrapani, B. Wei, A. Carrillo, P. M. Ajayan, R. S. Kane, *P. Natl. Acad. Sci. USA*, 2004, **101**, 4009-4012.
23. C. Py, R. Bastien, J. Bico, B. Roman, B. and A. Boudaoud, *Europhys. Lett.*, 2007, **77**, 44005.
24. P.-G. de Gennes, F. Brochard-Wyart, and D. Quèrè, *Capillarity and Wetting Phenomena*, 2004, Springer, New York.
25. B. S. Shvartsman, *J. Sound Vib.*, 2007, **304**, 969-973.
26. P. Grandgeorge, N. Krins, A. Hourlier-Fargette, C. Laberty-Robert, S. Neukirch, and A. Antkowiak, *Science*, 2018, **360**, 296.

27. P. Rothmund, A. Ainla, L. Belding, D. J. Preston, S. Kurihara, Z. Suo, and G. M. Whitesides, *Sci. Robot.*, 2018, **3**, eaar7986.
28. B. Pokroy, S. H. Kang, L. Mahadevan, and J. Aizenberg, *Science*, 2009, **323**, 237-240.
29. D. Chandra, S. Yang, A. Soshinsky, and R. Gambogi, *Acs Appl. Mater. Inter.*, 2009, **1**, 1698.
30. W. S. Wong, M. Li, D. R. Nisbet, V. S. Craig, Z. Wang, and A. Tricoli, *Sci. Adv.*, 2016, **2**, e1600417.
31. J. A. Faber, A. F. Arrieta, and A. R. Studart, *Science*, 2018, **359**, 1386-1391.
32. H. Lee, C. Xia, and N. X. Fang, *Soft Matter*, 2010, **6**, 4342.
33. B. Gorissen, D. Melancon, N. Vasios, M. Torbati, and K. Bertoldi, *Sci. Robot.*, 2020, **5**, eabb1967.